

Aerodynamics of Bridge Stay Cables Under Simultaneous Action of Rain and Wind – Part I: Vortex Shedding

Aerodinâmica de Cabos de Pontes Estaiadas Sob a Ação Simultânea de Chuva e Vento – Parte I: Desprendimento de Vórtices

D. S. MACHADO ^a
lac@ufrgs.br

A. M. LOREDO-SOUZA ^b
acir@ufrgs.br

Abstract

Simultaneous occurrence of cable vibrations under the combined action of wind and rain have been observed around the world in cable-stayed bridges in the last 20 years. This mechanism has caused great concern to bridge engineers and researchers due to the large vibration amplitudes. These vibrations, which are predominantly cross-wind, were observed only under conditions of light rain and low wind speed occurring simultaneously. This paper presents the main results of an experimental wind tunnel study on three sectional cable models, set to investigate the influence of rivulets on the vortex shedding mechanism. The M1 model was positioned horizontally with perpendicular wind incidence to the longitudinal axis, the M2 model was positioned horizontally with oblique wind to the longitudinal axis and the M3 model was a typical inclined cable of cable-stayed bridges. For the M3 model, the vortex shedding intensity increases for all rivulets positions. The greatest intensity occurred when the upper and lower rivulets were at 50° and 110°, respectively. For turbulent flow, the vortex shedding is stronger in the models with rivulets. For $Re < 1.2 \times 10^5$ the lower rivulets has no influence on the flow. However, for $> 1.2 \times 10^5$ the lower rivulets have a clear influence on the flow around the cylinder. For the inclined model (M3) the lower rivulet affected the flow for all the Re range.

Keywords: cable-stayed bridges, rain, wind, water rivulets.

Resumo

Simultâneas ocorrências de vibrações de cabos de pontes estaiadas sob ação combinada de chuva e de vento têm sido observadas ao redor do mundo nos últimos 20 anos. Este mecanismo tem causado grande preocupação aos engenheiros de pontes e pesquisadores por provocar grandes amplitudes de vibração. Estas vibrações, que são predominantemente transversais à direção do vento, foram observadas apenas sob condições de chuva leve e baixa velocidade do vento ocorrendo simultaneamente. Este trabalho apresenta os principais resultados de um programa experimental em túnel de vento, realizado com o intuito de investigar a influência dos filetes d'água formados na superfície dos cabos sobre o desprendimento de vórtices em três modelos seccionais. O modelo M1 foi posicionado horizontalmente com vento incidente normal ao eixo longitudinal, o modelo M2 foi posicionado horizontalmente com vento incidindo obliquamente ao eixo longitudinal e o modelo M3 representa um cabo inclinado típico de ponte estaiada. Para o M3 notou-se aumento da intensidade do desprendimento de vórtices para qualquer posição dos filetes. A maior intensidade ocorreu para os filetes superior e inferior localizados a 50° e 110°. Para escoamento turbulento, o desprendimento de vórtices é mais intenso nos modelos com filetes. Para $Re < 1,2 \times 10^5$ o filete inferior não tem influência sobre o escoamento. Entretanto, para $Re > 1,2 \times 10^5$ o filete inferior passa a afetar nitidamente o escoamento em torno do cilindro. Para o modelo inclinado o filete inferior apresentou influência no escoamento para todos os valores de Re .

Palavras-chave: pontes estaiadas, chuva, vento, filetes d'água.

^a Laboratório de Aerodinâmica das Construções, Universidade Federal do Rio Grande do Sul, lac@ufrgs.br, Caixa Postal 15.035 – CEP 91.501-970, Porto Alegre, Brasil;

1. Introduction

Currently, the cables of cable-stayed bridges have great flexibility, low mass and extremely low structural damping. Therefore, these cables are susceptible to vibration caused by various aerodynamic excitation mechanisms; among them a new kind of phenomenon known as wind-rain-induced vibrations. Cable vibrations of cable-stayed bridges under the combined action of rain and wind have been observed around the world in the last 20 years. This paper presents results obtained by measuring instantaneous external pressures in a cross section of a sectional model of a typical cable-stayed bridge with and without artificial rivulets. It was determined how the location of the rivulets influenced the position and intensity of vortex shedding in models with artificial rivulets as well as the influence of flow on the model with rivulets. Experimental investigations were carried out in the Joaquim Blessmann boundary layer wind tunnel of the Building Aerodynamics Laboratory (LAC) of the Federal University of Rio Grande do Sul (UFRGS).

1.1 Rationale

Large amplitudes reduce the service life of cables and their connections due to fatigue and therefore damage the corrosion protection duct. Moreover, the oscillations can also cause collisions between adjacent cables and cause user discomfort. It is necessary to understand the mechanisms of vibrations induced by rain and wind through field tests or wind tunnel investigation. The results presented below serve to improve the design of cable-stayed bridges.

2. Circular cylinders aerodynamics

2.1 Basic concepts

2.1.1 Pressure coefficients

The pressure coefficients are dimensionless coefficients obtained from the ratio of effective pressure, Δp , caused by wind in a small area on the surface of a body, and the dynamic pressure, q , Equation (1).

$$c_p = \frac{\Delta p}{q} \quad (1)$$

where c_p is the pressure coefficient, $q = \frac{1}{2} \rho_\alpha V^2$ [N/m²] is

the wind dynamic pressure corresponding to the average velocity measured at the middle of the sectional cable model, V the average wind velocity at the same position [m/s] and ρ_α is the air density [kg/m³].

2.1.2 Force coefficients

These coefficients are also dimensionless and depend on the shape of the cross section and the wind attack angle, β . Furthermore, they also depend on the flow regime and especially for cir-

cular sections they vary significantly with Reynolds number, Re . These force coefficients are:

a) Drag coefficient: coefficient related to the drag force that is the component of the global force in the flow direction (Equation 2);

$$C_D = \frac{F_D}{qD} \quad (2)$$

b) Lift coefficient: coefficient related to the lift force that is the component of global force perpendicular to the flow (Equation 3);

$$C_L = \frac{F_L}{qD} \quad (3)$$

where F_D is the average drag force per unit length [N/m], F_L is the average lift force per unit length [N/m] and D is the cable diameter [m].

2.1.3 Reynolds number, Re

The Reynolds number express a relation between the inertial forces and the viscosity forces (Equation 4).

$$Re = \frac{VD}{\nu} \quad (4)$$

where ν is the air cinematic viscosity.

2.1.4 Strouhal number, St

The frequency of vortex shedding is directly proportional to the wind velocity, being related through the Strouhal number (Equation 5), which usually depends on the geometry of the structure and the Reynolds number.

$$S_t = \frac{f_s D}{V} \quad (5)$$

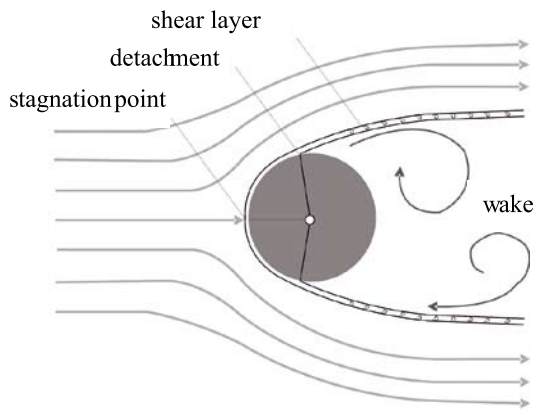
where f_s is the frequency of a pair of vortex shedding.

2.1.5 Vortex excitation

In non-aerodynamic bodies, a pair of vortex shedding appears at a specific Reynolds number range.

This is called Kármán vortex. The vortex shedding induces lateral forces perpendicular to the flow and consequently induces movements in this direction (Blessmann [1]). Figure 1 shows the characteristics of the flow around a stationary cylinder defining the shear layer, stagnation point, separation point, and wake.

Figure 1 – Flow around a circular cylinder



3. Inclined circular cylinder aerodynamics

Additional effects appear in inclined cylinders such as axial flow, with low-frequency vortex shedding, and rain-wind-induced vibrations. The position of the cable to the wind is defined in Figure 2. The inclination angles (the angle the cable makes with the horizontal plane) and the incidence angle (defined as the angle between the cable projection on the horizontal and a vertical plane perpendicular to the wind direction) are defined by α and β , respectively.

3.1 Axial flow

Matsumoto et al. [4] showed the existence of a strong axial flow near the wake along the axis of a yawed cylinder ($\alpha = 0^\circ$ and $\beta \neq 0^\circ$). The axial flow causes disturbance in the regular Kármán vortex shedding. Figure 3 shows the flow around a cylinder with $\alpha = 0^\circ$ e $\beta = 45^\circ$.

For inclined circular cylinders, it is possible to say that the axial flow near the wake has a feature similar to the separation plate submerged in the wake (Matsumoto [4]).

Figure 2 – (a) Definition of cable inclination, the incidence angle of the wind and the equivalent incidence angle of the wind (b) reference to incidence angle and aerodynamic forces (Phelan et al. (7))

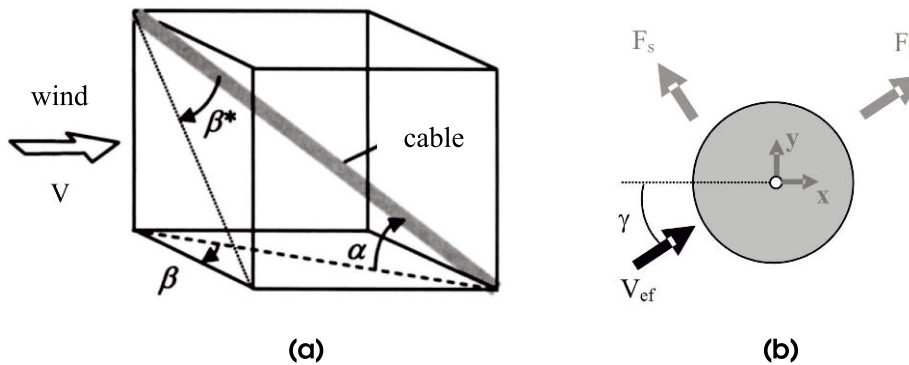


Figure 3 – Downstream axial flow at inclined cable (Matsumoto (3))

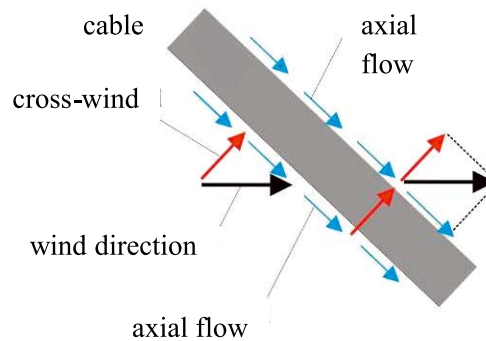
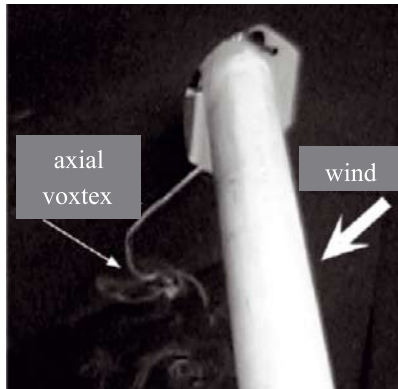


Figure 4 - Axial vortex view in the inclined cable wake ($\alpha=0^\circ$ e $\beta=45^\circ$, $V=0.5\text{m/s}$, smooth flow) (Matsumoto et al (5))



3.2 Low-frequency vortex

The low frequency vortex shedding is also known in the literature as axial vortex, vortex shedding of long period or vortex shedding with frequency lower than the Kármán vortex shedding. Matsumoto et al. [6] verified the existence of the axial vortex by using smoke to identify the formation of vortex in the wake of the cable as shown in Figure 4.

3.3 Rain-wind-induced vibrations

These vibrations are a new kind of instability phenomena (Matsumoto et al. [5]). These vibrations, which are predominantly cross-wind, were observed only under conditions of light rain and low wind velocity, occurring simultaneously. The oscillations are caused by the formation of two rivulets along the surface of the cables in the axial direction, which, due to its motion, constantly change the distribu-

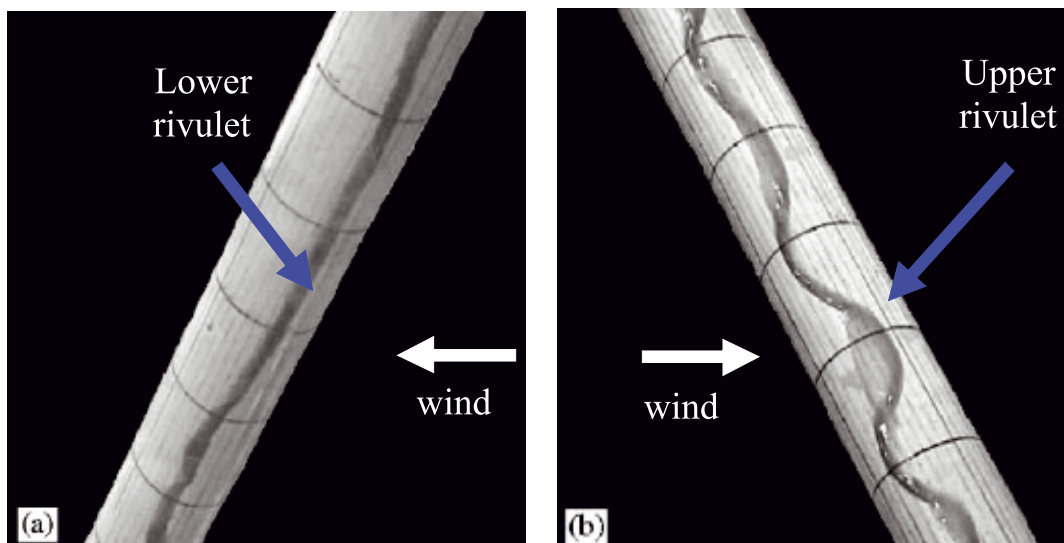
tion of pressures around the cables. Matsumoto et al. [5] observed double amplitude (peak to peak) on the Bridge Islands (Denmark) up to 2m due to the combined effect of rain and wind. Each rivulet is formed by a filament of rain water resulting from precipitation on the cables (Figure 5). They are called lower rivulet (Figure 5a) and upper rivulet (Figure 5b). The formation of the upper fillet can take a sine wave form (Wang et al. [10]). The position of the lower and the upper rivulets is identified in this paper by θ_1 e θ_2 , respectively in Figure 6, where V_{ef}^1 is the velocity on the cable's normal plane and γ is the attack angle perpendicular to the section.

The rivulets' position varies almost linearly with wind velocity. Hikami and Shiraishi [3] showed that the occurrence of vibrations induced by rain and wind is limited to cables geometrically inclined against the wind. The largest amplitudes of vibration induced by wind and rain occur for cable inclinations between 25° and 45° and incidence angles between 30° e 45° . The vibrations that reach large amplitudes occur only in the presence of light to moderate rain (rain intensity of about 8 mm / h (Ni et al. [7])). Water rivulets oscillate over the surface of cables in the circumferential direction. This movement is mainly caused by the temporary acceleration of the cross section. The rivulets' movement is influenced by the fluid-structure interaction and the forces acting on them. The change in rivulets' position causes a continuous variation of the cross section cable shape, which leads, in turn, the variation of force coefficients (Verwiebe [9]). The rivulets oscillate with the same frequency of the cable movement (Hikami and Shiraishi [3]).

3.3.1 Experimental investigation

Three stationary sectional models of a typical cable-stayed bridge were covered with artificial rivulets having geometric scale of 1:1 identified as M1, M2 and M3. The models represent the corrosion protection duct of steel tendons that make up a typical system of cables in a cable-stayed bridge. Figure 7 is a cross section scheme of the corresponding model. Figure 10 shows a schematic view of the positioning of the three models tested in the wind tunnel. The water rivulets have a semi-elliptical cross section (rivulet width $b_{ri}=13$ mm and rivulet height $h_{ri}=5$ mm) and were made using a

Figure 5 - Water rivulets view along the cable: (a) lower rivulet (leeward) and (b) upper rivulet (windward) (Wang et al. (9))



¹ A cable under wind effect with velocity V , will have a inclination α with horizontal plane and incidence angle β . For geometric definition the effective velocity – function of V , α and β - acts perpendicular to the cable at a wind attack angle γ to normal cable section. For calculation details of V_{ef} and γ see Phelan et al. [8].

Figure 6 – (a) Representation of the rivulets position on a typical cable-stayed bridge section and (b) definition of the upper and lower rivulets position

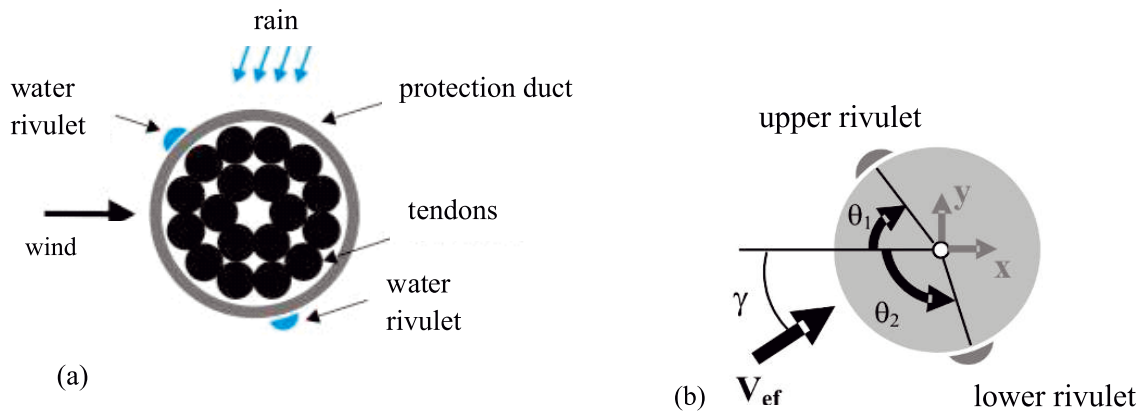
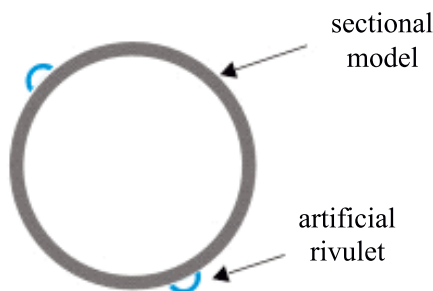


Figure 7 – Example of sectional model



plastic tube cut in the longitudinal (Figure 8). The rivulets' length are the same as the models length. Figure 9 shows the pressure taps distribution on the sectional cable model. Instantaneous pressures around of the cable's cross section

were measure in the mid-span with and without the presence of rivulets, under different circumstances. Measurements were made using electronic pressure transducers. The M1 model was positioned horizontally ($\alpha = 0^\circ$) and with wind incidence angle ($\beta = 0^\circ$). The M2 model was positioned horizontally ($\alpha = 0^\circ$), however with wind incidence angle ($\beta = 30^\circ$). The M3 model was positioned inclined ($\alpha = 45^\circ$) and with wind incidence angle ($\beta = 30^\circ$). Figure 10 shows the models in the wind tunnel test chamber.

For the generation of turbulent wind a grid capable to generating turbulence intensity of 10.5% was used. Table 1 shows the variable test parameters.

Power Spectral Density (PSD) functions of the instantaneous force coefficients obtained from the external pressure measurements were determined. Pressure taps were used to measure the external pressure. The instantaneous drag and lift coefficients were obtained from the integration of the instantaneous external pressure measurements. The spectra are presented by $S(f) \times 1000 [1/Hz]$ as a function of the reduced frequency fD/V for clarity in the analysis. The following observations were made from the results obtained.

M1 model: Figures 11 and 12 present the PSD of C_L (PSD of instantaneous lift coefficients) and the PSD of C_D (PSD of instantaneous drag coefficients) under a smooth flow ($Re \cong 7.7 \times 10^4$)

Figure 8 – Perspective (a) and cross-section (b) of the artificial rivulets for the wind tunnel models

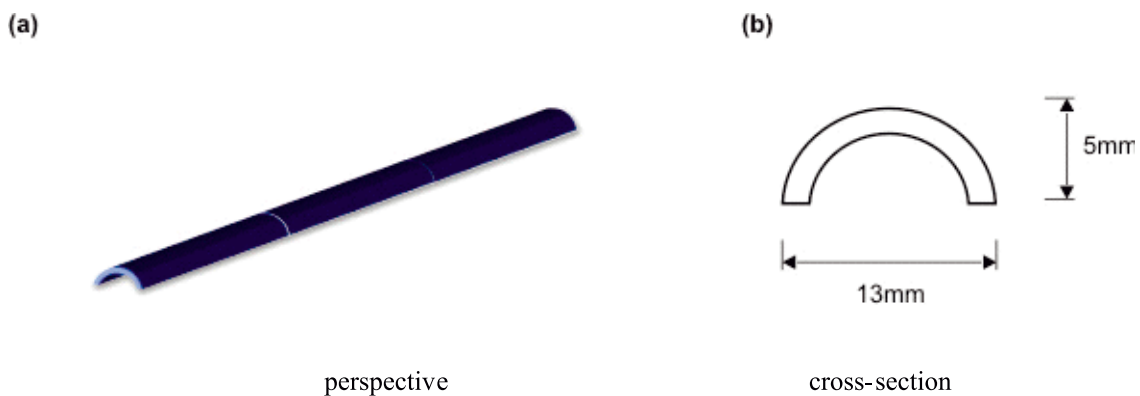
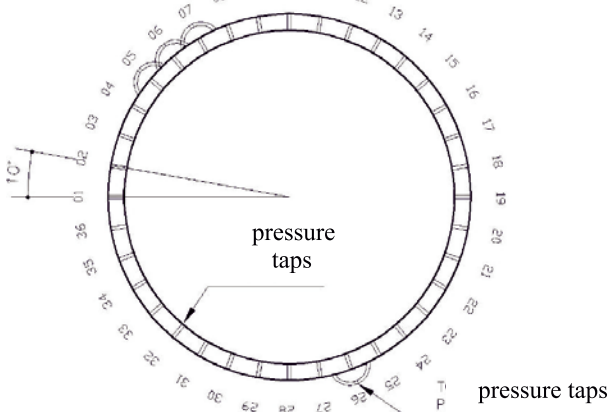


Figure 9 - Location and distribution of pressure taps in the model



applied to the configurations SF (cable without rivulets), F40 (cable with rivulets at $\theta_1 = 40^\circ$ and $\theta_2 = 110^\circ$), F50 (cable with rivulets at $\theta_1 = 50^\circ$ and $\theta_2 = 110^\circ$) and F60 (cable with rivulets at $\theta_1 = 60^\circ$ and $\theta_2 = 110^\circ$). Other researchers also observed maximum amplitudes at $Re \cong 7.7 \times 10^4$ [2].

For a normal circular cylinder (without rivulets), the characteristic spectra for drag and lift will present a frequency ratio of two, that is, the alternating transversal forces will occur in the shedding frequency of a pair of vortices, while in the along-wind direction the alternating forces will occur in the frequency of an individual vortex [1]. This can be clearly seen in figures 11a and 12a. When the rivulets are present, note that a second, lower frequency, peak appears in the spectra. This is probably due to the shedding of the vortices from the upper rivulets which are registered in their individual frequencies.

Figure 13 shows the PSD at pressure taps which present representative energy peaks for model M1 without rivulets in smooth flow, $Re \cong 7.7 \times 10^4$.

Figure 13 shows that the highest peaks occur at pressure taps 8 and 30 (see figure 10), which are symmetrical to the horizontal sections axis. Due to the higher energy achieved, these positions represent the vortex detachment location in the model without fillets.

Figure 10 - Placement of M1, M2 and M3 models in the wind tunnel test chamber

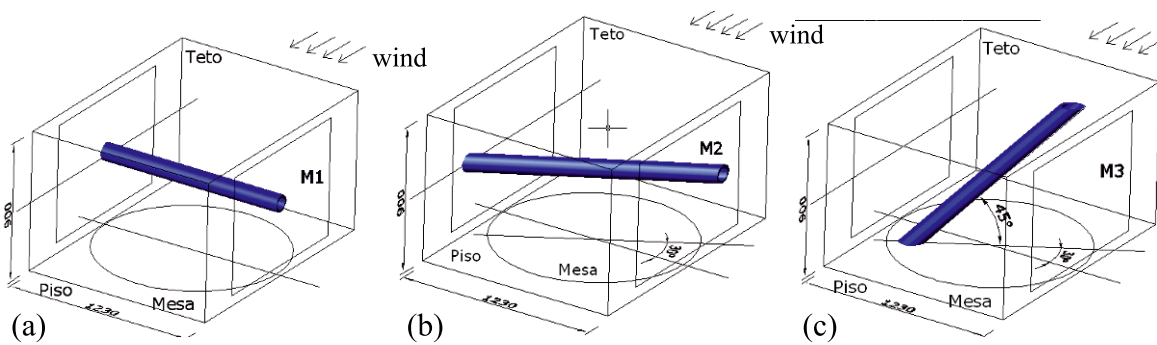


Figure 11 - PSD from lift coefficients time history (a) SF, (b) F40, (c) F50, (d) F60, for $Re \cong 7.7 \times 10^4$, smooth flow, M1

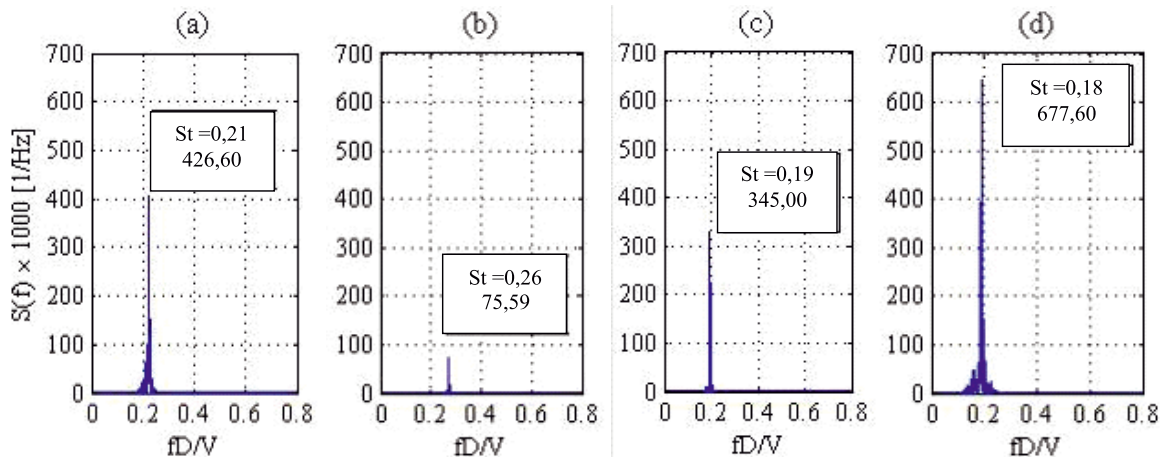


Figure 12 – PSD from drag coefficients time history (a) SF, (b) F40, (c) F50, (d) F60, for $Re \cong 7.7 \times 10^4$, smooth flow, M1

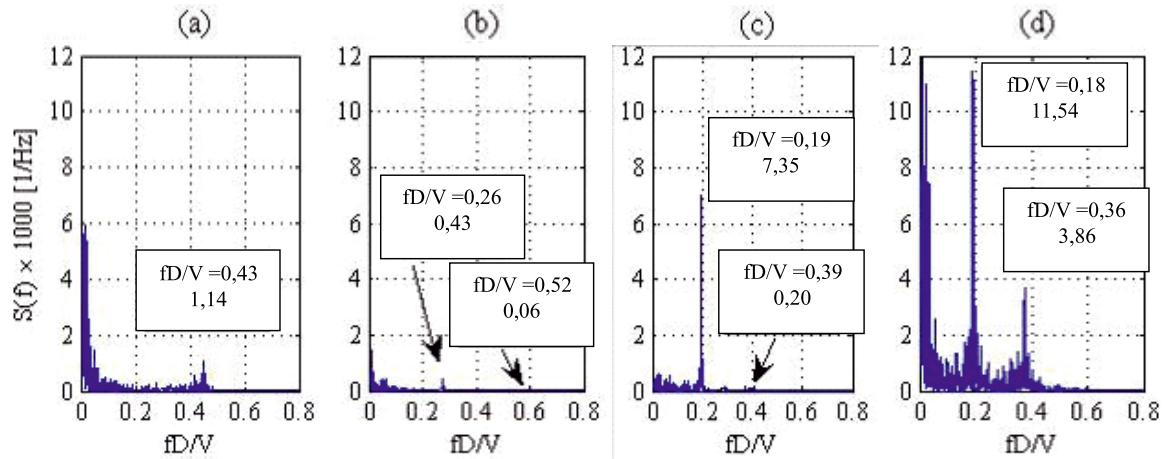
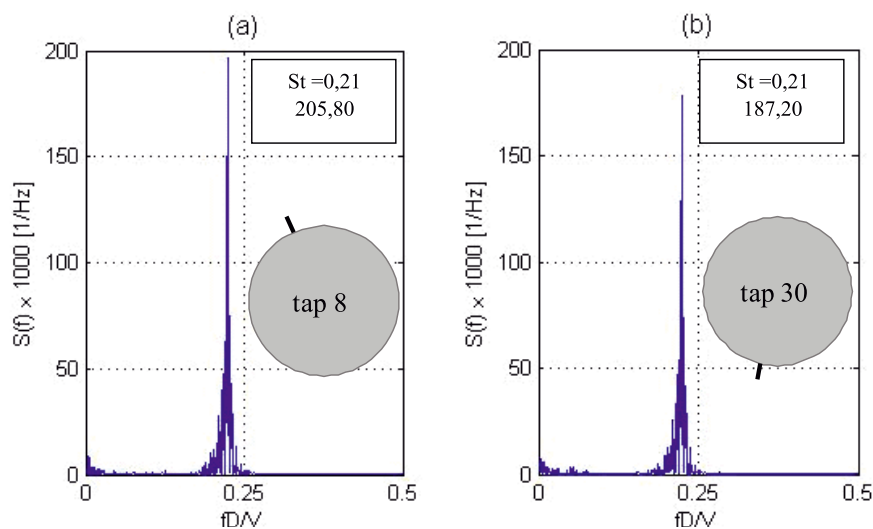


Figure 14 shows the PSD on some pressure taps which present representative energy peaks for model M1 at setting F40 with a smooth flow, $Re \cong 7.7 \times 10^4$. Observe in Figure 14 that the PSD peak intensity on pressure tap 5 (upper rivulet) is highest than on tap 4; in pressure tap 7 PSD peak intensity decreases and after increases in 11. A vortex shedding occurs on the upper rivulet (stronger intensity) with flow reattachment on pressure tap 7 (weaker intensity) and new detachment at 11 (stronger intensity). At the bottom of the model the vortex shedding occurs at pressure tap 29. Figure 15 shows the external pressure PSD on the pressure taps 5, 6 and 30 which present representative energy peaks for model M1 at setting F50 with a smooth flow, $Re \cong 7.7 \times 10^4$. Observe the vortex shedding on upper rivulet (tap 6). At the bottom of the cable the vortex shedding occurs on pressure tap 30. Figure 16 shows the external pressure coefficients PSD on pressure taps 6, 7 and 30 which present representative energy peaks for model

M1 at setting F60 with a smooth flow, $Re \cong 7.7 \times 10^4$. Observe in Figure 16 the vortex shedding occurs on upper rivulet (tap 7). At the cable bottom the vortex shedding occur on pressure tap 30. According to Figures 11 to 16, it was observed that: for setting F40 the Strouhal number or reduced frequency (fD/V) is larger than for setting SF, while for setting F50 and F60 the fD/V value is less than for the SF (no rivulet) case. At setting F40, the peaks have lower intensity compared to the other configurations. At setting F50, note an increase in the intensity of the vortex shedding and reduction of the reduced frequency compared to the settings SF and F40. Observe in the $S(f)$ of C_D (Figure 12c) the second harmonic almost disappears. The upper rivulet appears to suppress the vortices on one side of the model making the $S(f)$ of C_L (Figure 11c) coincide with the $S(f)$ of C_D . The along-wind response has the same frequency of the cross-wind response, but with lower intensity. At setting F60, both $S(f)$

Figure 13 – PSD from external pressure time history (a) tap 8, (b) tap 30, for $Re \cong 7.7 \times 10^4$, smooth flow, M1, SF



of C_D and $S(f)$ of C_L , peaks had higher intensity than the model without rivulets.

When the upper rivulet is in position $\theta_1 = 60^\circ$ an increase of vortex shedding intensity on the rivulet may occur. The peaks with dif-

ferent reduced frequencies $S(f)$ of C_D (Figure 12d) indicate different intensities of vortex shedding on each side of the model. Figure 17 shows a scheme of vortex shedding on M1 model at settings, SF, F40, F50 e F60. At Figure 17, the vortices show where the highest

Figure 14 – PSD from external pressure time history (a) tap 4, (b) tap 5, (c) tap 7, (d) tap 11, (e) tap 29, (f) tap 26, for $Re \cong 7.7 \times 10^4$, M1, F40

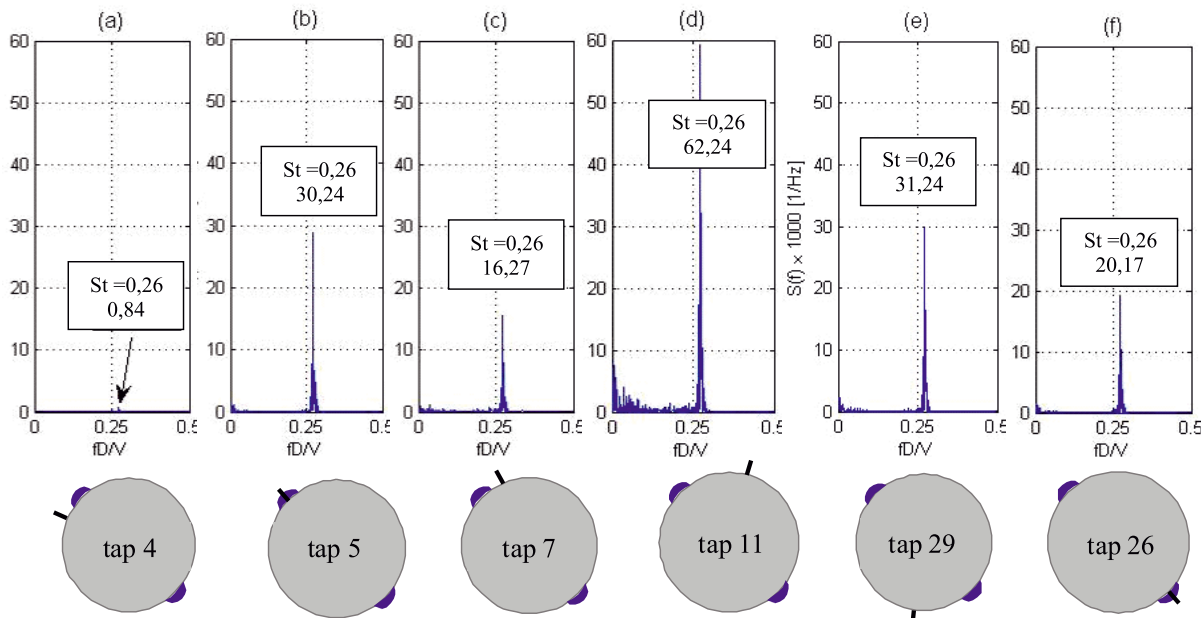
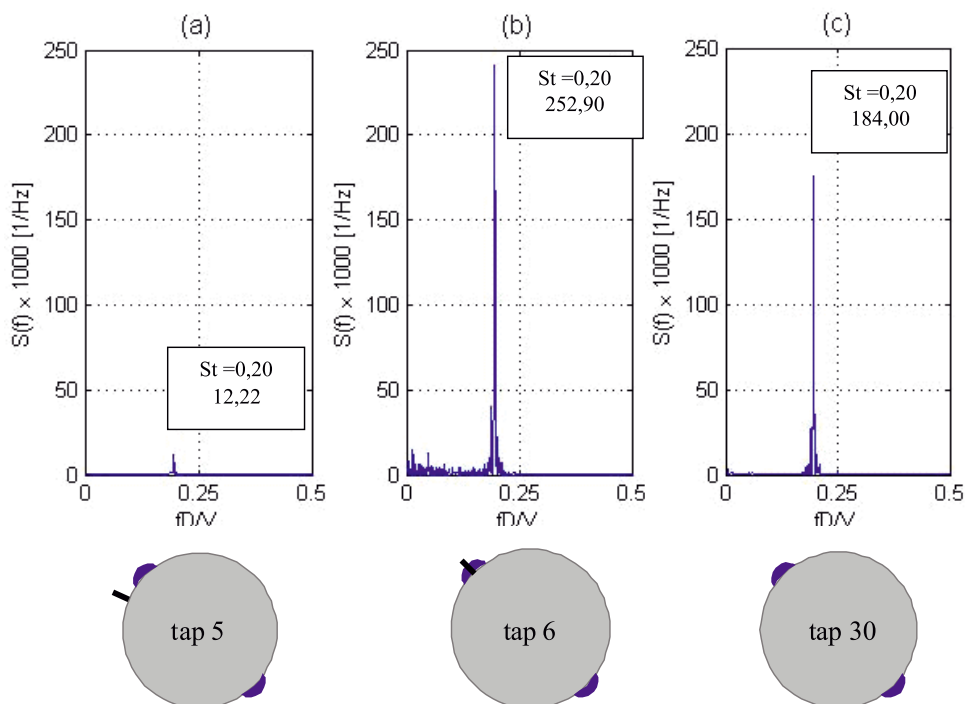


Figure 15 – PSD from external pressure time history (a) tap 5, (b) tap 6, (c) tap 30, with smooth flow, $Re \cong 7.7 \times 10^4$, M1, F50



intensity of PSD peaks of C_D occurred, with its respective value of $S(f) \times 1000$.

For Reynolds numbers higher than $Re \approx 7.7 \times 10^4$, it is possible to identify the lower rivulet influence on vortex shedding.

M2 model: In this model it was only possible to identify peaks for Re between 3.9×10^4 and 1.2×10^5 , for both smooth and turbulent flow. At high values of Re , the PSD of drag and lift coefficients present a broad band spectrum with less defined peaks. At settings with rivulets the spectral peaks were more defined, but with

lower intensity than in the model without rivulets. In the $S(f)$ of C_D , it was not possible to identify pronounced peaks. In the model under turbulent flow and the presence of rivulets, the peaks in $S(f)$ of C_L were higher than in the model under smooth flow. For the model without rivulets under turbulent flow, the peaks were lower than under smooth flow.

M3 model: The same observations made for model M2 in the previous paragraph are valid for model M3.

General considerations: Figures 18 to 20 show the PSD (with

Figure 16 – PSD of external pressure time history (a) tap 6, (b) tap 7, (c) tap 30, for $Re \cong 7.7 \times 10^4$, M1, F60

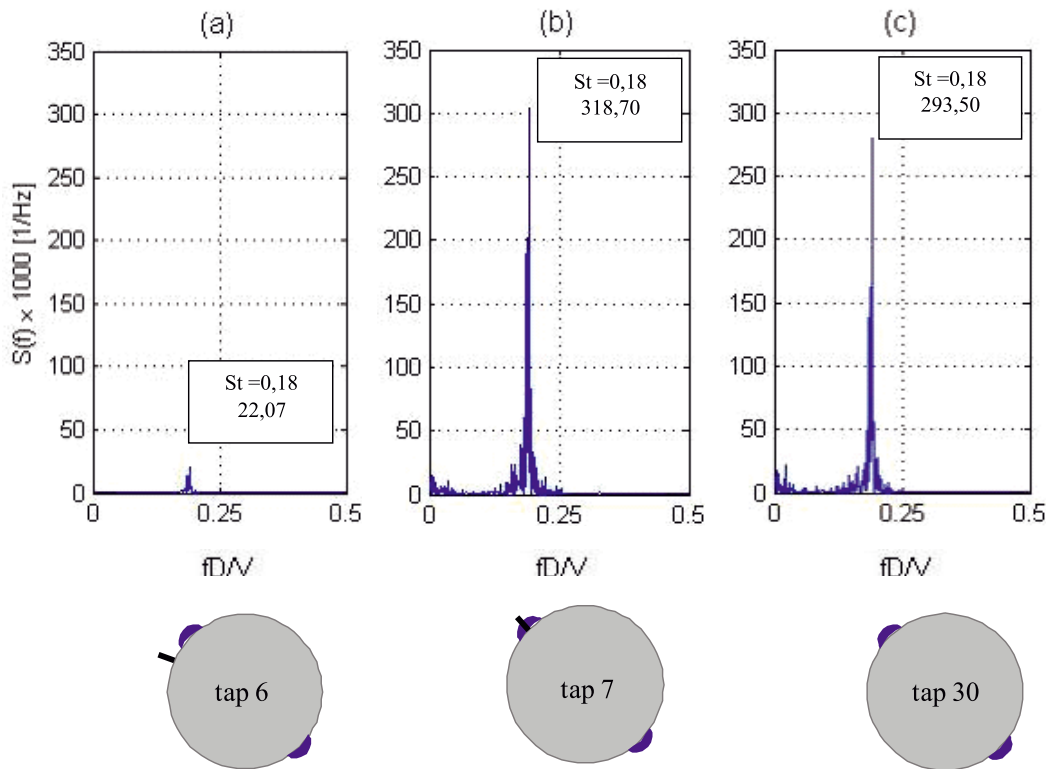
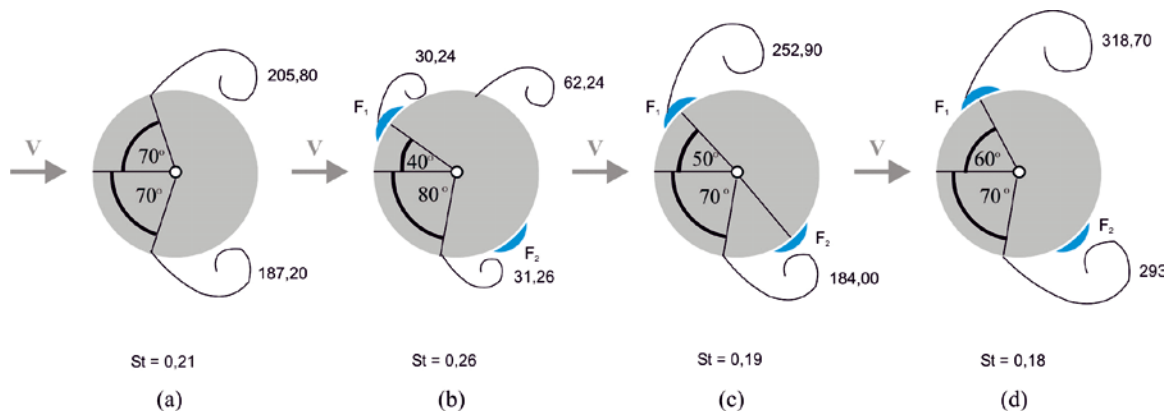


Figure 17 – Scheme of vortex shedding on M1 model for all settings



their values St and $S(f)$ for lift coefficient time history for all models and settings, under turbulent flow for $Re \cong 7.7 \times 10^4$.

Observe that in model M1 at settings F40 and F50 the peaks are stronger than at settings SF, and F60 (Figure 18a, b, c, d) unlike the smooth flow situation, in that F60 presented the highest peaks (Figure 12d). The reduced frequencies (Strouhal numbers) decrease as the positions of the models in the wind tunnel change from M1 to M2 and than to M3. Model M3 presented the highest peak at setting F50, and settings F40 and F60 presented peaks with the same intensities. Note that the reduced frequencies (Strouhal numbers) for model M3 were lower than on the other models. The low value of fD/V can be caused by the axial vortex effect that can occur on inclined cables at lower frequencies than the Kármán vortex shedding. Observe that the presence of rivulets on M3 model increases the vortex shedding intensity.

4. Conclusions

From the analysis of the results it was possible to draw the following conclusions:

- the flow separation for the inclined cables occurred on the rivulets;
- at horizontal models, the presence of rivulets can eliminate or amplify the intensity of vortex shedding depending on the rivulets location;
- model M3 showed an increase in the intensity of vortex shedding for any rivulet position, but the intensity was highest for F50;
- for turbulent flow the vortex shedding is stronger in the models with rivulets;

Figure 18 – PSD of lift coefficients time history with turbulent flow, M1 model (a) SF, (b) F40, (c) F50, (d) F60, $Re \cong 7.7 \times 10^4$

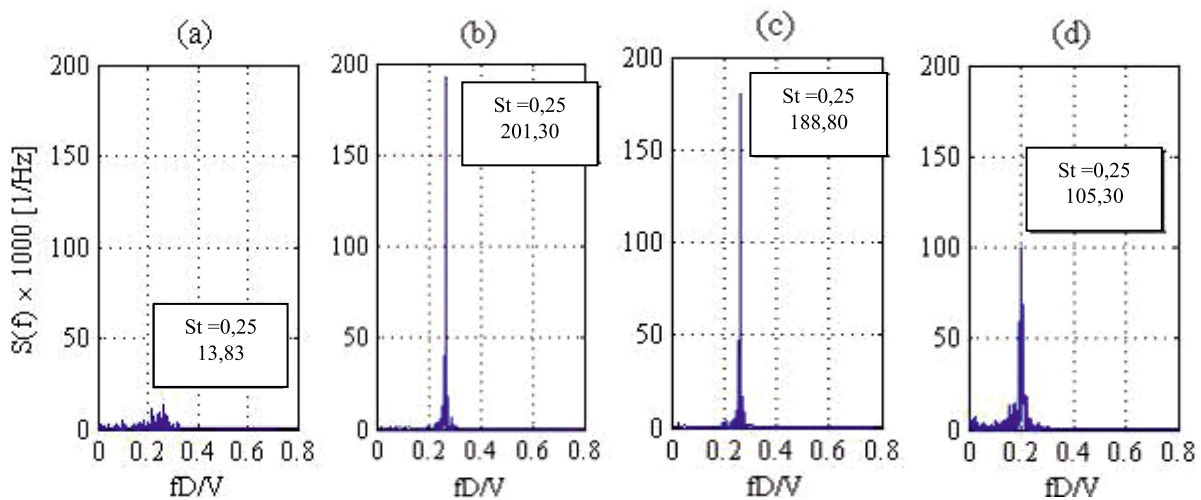


Figure 19 – PSD of lift coefficients time history with turbulent flow, M2 model (a) SF, (b) F40, (c) F50, (d) F60, $Re \cong 7.7 \times 10^4$

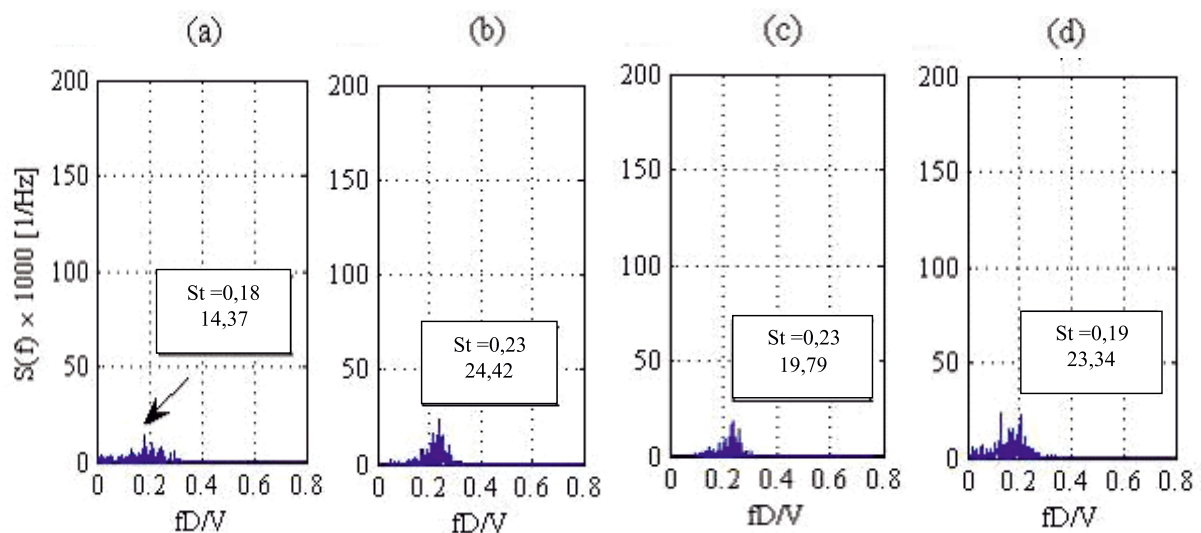
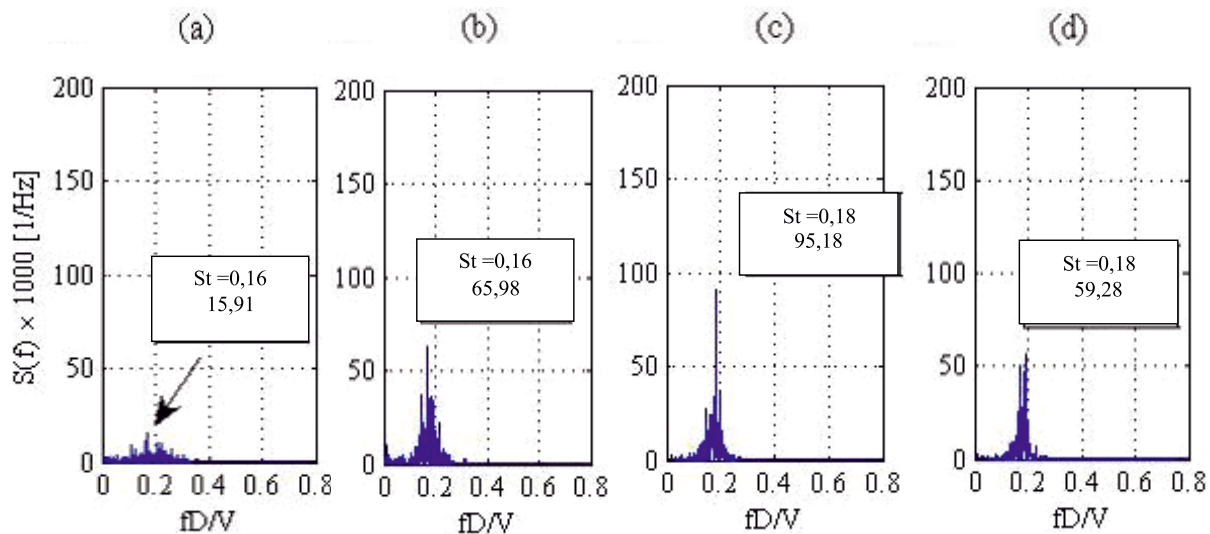


Figure 20 – PSD of lift coefficients time history with turbulent flow, M3 model (a) SF, (b) F40, (c) F50, (d) F60, to $Re \cong 7.7 \times 10^4$



- regardless of the rivulets' presence, the inclined model (M3) had frequencies of vortex shedding lower than those obtained by conventional Kármán vortex. It is a possible effect of the axial vortex;
- for the horizontal models, the lower rivulet has no influence on the flow for Re below 1.2×10^4 . At Re above 1.2×10^4 , the lower rivulet has a clear influence on the flow. For the inclined models, the lower rivulet influenced the flow for all Re values.

5. Acknowledgments

The authors acknowledge the valuable help of CAPES for the completion of this research, as well as all the LAC/UFRGS staff, where the tests were performed.

6. References

- [01] BLESSMANN, J. Introdução ao estudo das ações dinâmicas do vento. 2ª ed. Porto Alegre: Ed. da UFRGS, 2005. 282p.
- [02] GU, M., DU, X. Experimental investigation of rain-wind-induced vibration of cables in cable-stayed bridges and its mitigation. *Journal of Wind Engineering and Industrial Aerodynamics*. Elsevier Science Publisher, 2005. v.93, p.79-95.
- [03] HIKAMI, Y., SHIRAISHI, N. Rain-wind induced vibrations of cables in cable stayed bridges. *Journal of Wind Engineering and Industrial Aerodynamics*. Elsevier Science Publisher, 1988. v.29, p.409-418.
- [04] MATSUMOTO, M., SHIRAISHI, N., KITAZAWA, M., KNISELY, C., SHIRATO, H., KIM, Y., TSUJJI, M. Aerodynamic behavior of inclined circular cylinders-cable aerodynamics. *Journal of Wind Engineering and Industrial Aerodynamics*. Elsevier, 1990. v.33, p.63-72.
- [05] MATSUMOTO, M., SHIRAISHI, N., SHIRATO, H. Rain-wind induced vibration of cables of cable-stayed bridges. *Journal of Wind Engineering and Industrial Aerodynamics*. Elsevier Science Publisher, 1992. v.41-44, p.2011-2022.
- [06] MATSUMOTO, M., YAGI, T., SHIGEMURA, Y., TSUSHIMA, D. Vortex-induced cable vibration of cable-stayed bridges at high reduced wind velocity. *Journal of Wind Engineering and Industrial Aerodynamics*. Elsevier Science Publisher, 2001, v.89, p.633-647.
- [07] NI, Y. Q., SHIRATO, H., YAGI, T., GOTO, M., SAKAI, S., OHYA, J. Field observation of rain-wind-induced cable vibration in cable-stayed Dongting Lake bridge. *Journal of Wind Engineering and Industrial Aerodynamics*. Elsevier Science Publisher, 2007, v.95, p.303-328.
- [08] PHELAN, R. S., SARKAR, P. P., MEHTA, K. C. Full-scale measurements to investigate rain-wind induced cable-stay vibration and its mitigation. *Journal of Bridge Engineering*. American Society of Civil Engineering, 2006. v.11, p. 293-304.
- [09] VERWIEBE, C. Rain-wind-induced vibrations of cables and bars. In: *Proceedings of International Symposium on advances in bridge aerodynamics*. Copenhagen, Denmark. May, 1998. pp.255-263.
- [10] WANG, Z. J., ZHOU, Y., HUANG, J. F., XU, Y. L. Fluid dynamics around an inclined cylinder with running water rivulets. *Journal of Fluids and Structures*. Elsevier Science Publisher, 2005. v.21, p.49-64.